Lawrence Berkeley National Laboratory

Title
Enhancing ferroelectric photovoltaic effect by polar order engineering

Authors
You, Lu
Zheng, Fan
Fang, Liang
et al.

APPLIED PHYSICS

Enhancing ferroelectric photovoltaic effect by polar order engineering

Lu You[1]*, Fan Zheng[2]*†, Liang Fang[3]*, Yang Zhou[1], Liang Z. Tan[2], Zeyu Zhang[4], Guohong Ma[4], Daniel Schmidt[5]‡, Andrivo Rusydi[5], Le Wang[1]§, Lei Chang[1], Andrew M. Rappe[2]¶, Junling Wang[1]¶

Ferroelectric materials for photovoltaics have sparked great interest because of their switchable photoelectric responses and above-bandgap photovoltages that violate conventional photovoltaic theory. However, their relatively low photocurrent and power conversion efficiency limit their potential application in solar cells. To improve performance, conventional strategies focus mainly on narrowing the bandgap to better match the solar spectrum, leaving the fundamental connection between polar order and photovoltaic effect largely overlooked. We report large photovoltaic enhancement by A-site substitutions in a model ferroelectric photovoltaic material, $BiFeO_3$. As revealed by optical measurements and supported by theoretical calculations, the enhancement is accompanied by the chemically driven rotational instability of the polarization, which, in turn, affects the charge transfer at the band edges and drives a direct-to-indirect bandgap transition, highlighting the strong coupling between polarization, lattice, and orbital order parameters in ferroelectrics. Polar order engineering thus provides an additional degree of freedom to further boost photovoltaic efficiency in ferroelectrics and related materials.

INTRODUCTION

The discovery of photovoltaic effect in ferroelectric materials can be traced back to more than 50 years ago (1–3). In contrast to classical semiconductor solar cells, photoexcited carriers in ferroelectric materials are spontaneously separated due to the inversion symmetry breaking. The fundamentally different mechanism endows ferroelectric photovoltaics (FPV) with unique characteristics, such as switchable photovoltaic outputs (4–7), above-bandgap photovoltage (2, 3, 8–10), and light polarization dependence (3, 4, 10, 11). Unfortunately, the large energy mismatch between the bandgaps of ferroelectric oxides and the solar spectrum makes them poor light absorbers with low power conversion efficiency and, particularly, low photocurrent. Recently, bandgap engineering via chemical substitution and ordering has been extensively explored and proven efficient in improving the FPV performance (12–16), which holds great promise for practical integration in next-generation optoelectronic devices. However, microscopic physics of the FPV effect remains poorly understood and controversial. Different mechanisms have been proposed to account for experimental results in various sample forms and device architectures, for example, polarization-dependent interfacial band bending (6, 17), bulk depolarization field (5), asymmetric momentum distribution of the nonequilibrium carriers (18), and shift current through coherent evolution (19–21). The general rule based on existing reports is that the interface effect dominates in vertically sand-wiched thin-film capacitors, while in bulk samples or thin-film samples with planar electrodes, the FPV is driven by bulk mechanism.

Regardless of the microscopic model, polar order is believed to lie at the core of the FPV effect. Furthermore, it is well known that interactions between polarization, lattice, and orbital order parameters in ferroelectric materials lead to enhancement of their physical properties near phase boundaries. One notable example is the huge electromechanical response resulting from phase and polar instability at the morphotropic phase boundaries in relaxor ferroelectrics (22). How polar instability would affect the FPV effect, however, remains largely unknown. Here, we modify the polar order in a prototypical FPV material, $BiFeO_3$ (BFO), by A-site substitutions. Intriguingly, we observe large photovoltaic enhancement for compositions near the boundary between the polar and nonpolar phases. Optical absorption spectra and time-resolved reflectivity spectroscopy reveal a consistent picture, that chemical substitution leads to a direct-indirect bandgap transition and consequently a longer carrier lifetime, conclusions that are supported by theoretical calculations. This subtle change around the band edges is closely related to the charge transfer (CT) affected by the polar instability through the cross-coupling between polarization, lattice, and orbital degrees of freedom. The improvement of FPV performance is also found for various lanthanide element substitutions, suggesting the generality of this polar order engineering approach, which offers a new design strategy for FPV and related materials.

RESULTS

Polar instability induced by chemical substitution in BFO

BFO is a CT insulator, with the band edges mainly defined by the mixing of the O 2p and Fe 3d orbitals. Therefore, isovalent A-site substitution of the Bi^{3+} does not directly affect the electronic structure close to the band edges. But it strongly influences the stability of the polar order by quenching the stereochemical activity of the Bi^{3+} 6s lone pair, which is believed to be the driving force for the ferroelectricity in BFO (23). A ferroelectric-paraelectric (FE-PE) phase transition can thus be induced by A-site lanthanide element substitution (24). Following this scheme, monodomain La-doped BFO films were epitaxially grown on

[1]School of Materials Science and Engineering, Nanyang Technological University, Singapore 639798, Singapore. [2]Department of Chemistry, University of Pennsylvania, Philadelphia, PA 19104–6323, USA. [3]Jiangsu Key Laboratory of Thin Films and Department of Physics, Soochow University, Suzhou 215006, China. [4]Department of Physics, Shanghai University, Shanghai 200444, China. [5]Singapore Synchrotron Light Source, National University of Singapore, 5 Research Link, Singapore 117603, Singapore.
*These authors contributed equally to this work.
†Present address: Joint Center for Artificial Photosynthesis and Materials Sciences Division, Lawrence Berkeley National Laboratory, Berkeley, CA 94720, USA.
‡Present address: GLOBALFOUNDRIES, Albany, NY 12203, USA.
§Present address: Environmental Molecular Sciences Laboratory, Pacific Northwest National Laboratory, Richland, WA 99352, USA.
¶Corresponding author. Email: jlwang@ntu.edu.sg (J.W.); rappe@sas.upenn.edu (A.M.R.)

vicinal SrTiO$_3$ (STO) substrates (7), and comprehensive ferroelectric characterizations were carried out (see Materials and Methods). As shown in the polarization (P-E) and dielectric hysteresis loops (Fig. 1, A and B), the ferroelectric state is preserved for La substitution up to 20%. However, with 30% La, clear double-hysteresis behavior starts to appear in the P-E loop, which correlates with the quadruple-humped dielectric loop. Further increase of the La concentration leads to the collapse of the hysteresis loop with strongly suppressed remnant polarization, a signature of phase evolution toward paraelectric state. By plotting the remnant polarization (P$_r$) and the relative permittivity (ε_r) against the La concentration (see figs. S1 and S2 for details), a transition from ferroelectric phase (high P$_r$, low ε_r) to paraelectric phase (low P$_r$, high ε_r) is evident, with a relatively wide crossover region (Fig. 1C).

To gain a deeper understanding of the FE-PE phase transition at the mesoscopic scale, we used piezoelectric force microscopy (PFM) to probe the local ferroelectric domain evolution upon La substitution (see Materials and Methods). Figure 1 (D and F) shows the out-of-plane PFM responses of the pure and 20% La–substituted BFO films in the as-grown state, respectively. Pure BFO displays a monodomain state with a homogeneous piezoresponse representing upward polarization. When 20% of the Bi is substituted by La, a large number of domains with greatly suppressed piezoresponse start to nucleate from the polar matrix, indicating the coexistence of polar and nonpolar phases in the film, which is in accordance with the intermediate state of ferroelectric-antiferroelectric mixtures before entering the paraelectric state (25). When the La concentration is increased to 40%, no
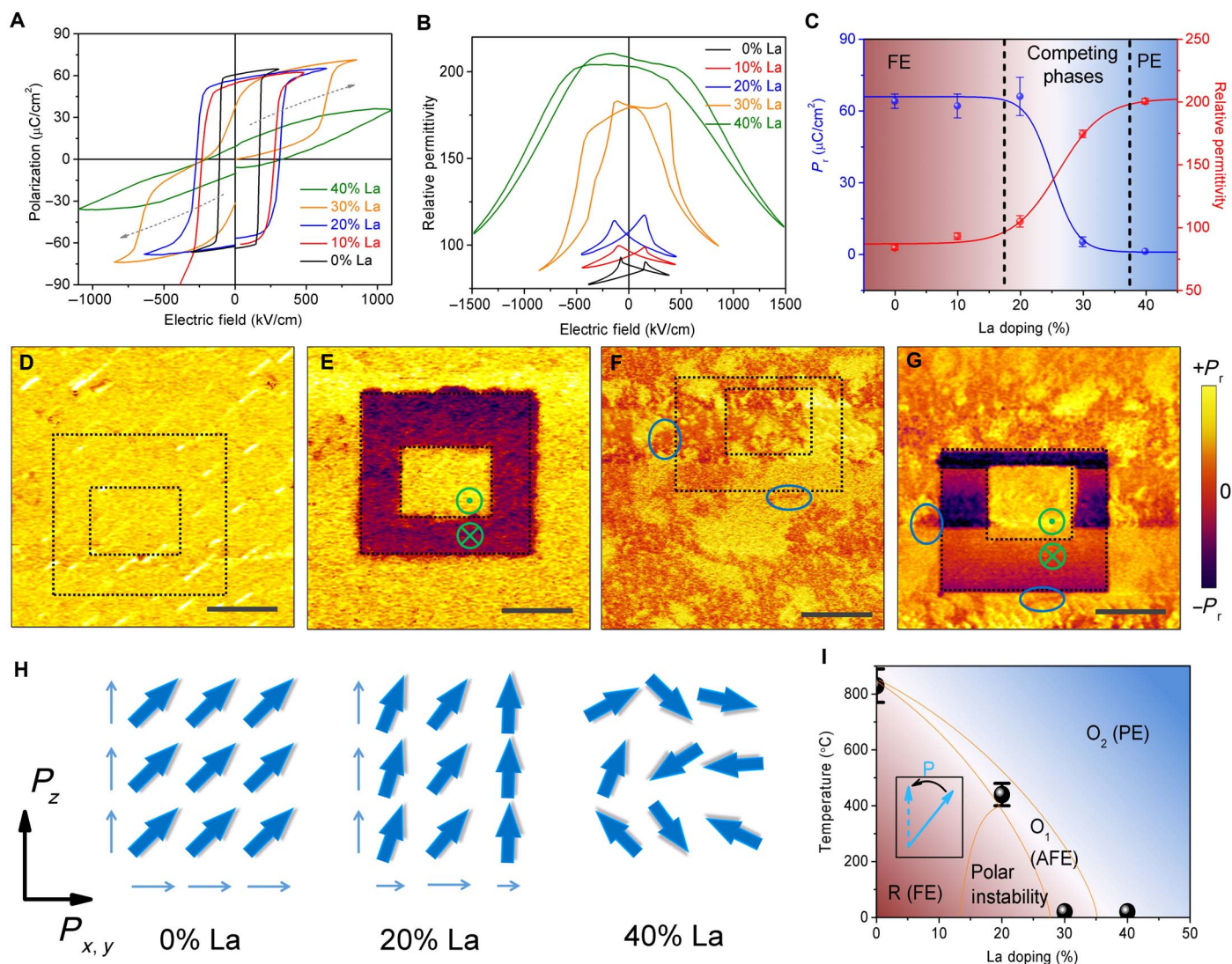

Fig. 1. Polar instability of BFO induced by chemical substitution. (**A**) Polarization and (**B**) relative permittivity hysteresis loops of La-substituted BFO films. (**C**) Evolution of remnant polarization and relative permittivity versus La concentration showing FE-PE phase transition. Piezoresponse images of (**D**) pure and (**F**) 20% La–substituted BFO films in as-grown states. (**E** and **G**) Piezoresponse images after writing box-in-box patterns, as depicted by the dashed squares in (D) and (F), respectively. The blue circles indicate the same locations before and after switching. The scale bar is 1 μm for all PFM images. (**H**) Simplified schematic representing the polarization states of the La-substituted films after electrical poling. (**I**) Brief temperature-composition phase diagram indicating the competing polar instability caused by the substitution of Bi by La. R, rhombohedral-like phase; O$_1$, AFE orthorhombic phase; O$_2$, PE orthorhombic phase. The region in between FE and AFE shows polar instability.

piezoresponse can be detected, suggesting a paraelectric ground state (fig. S3). This observation, however, seems contradictory to the fully saturated P-E loop of the 20% La–substituted film, as shown in Fig. 1A. To clarify the discrepancy, we conducted local polarization switching by applying opposite dc biases to the scanning tip, producing box-in-box patterns (as shown in Fig. 1, E and G; see also fig. S4). As expected, pure BFO shows classical 180° polarization reversal, in agreement with its single ferroelastic state, while, surprisingly, the mixture of polar and nonpolar regions in 20% La–substituted BFO is converted into uniformly polarized states after electrical poling. This means that the electric field can align the dipoles and stabilize the ferroelectric phase in the film, which explains the fully saturated P-E loop. It also signifies the near degeneracy of polar and nonpolar phases at 20% La substitution. In-plane PFM signals provide additional information (fig. S4). First, the overall reduction of the in-plane piezoresponse upon La doping indicates the suppression of the in-plane polarization component. That is, the polarization continuously rotates toward surface normal (26). Second, La–doped BFO samples exhibit inhomogeneous contrast even after electrical poling, which points to the rotational instability of the polarization induced by La substitution. The polarization states of different La-substituted BFO compositions after electrical poling are thus illustrated in Fig. 1H. Between the completely ordered FE and disordered PE states, intermediate La-substituted samples exhibit suppressed in-plane polarization and incommensurate domains with rotational instability.

On the basis of the above observations, a temperature-composition phase diagram can be charted for La-substituted BFO (Fig. 1I). The Curie temperature T_C for each composition is empirically determined by extrapolating the coercive field of the P-E loop to zero (fig. S5). The phase diagram shown here is in agreement with those reported in the literature for lanthanide element–substituted BFO (27–29). In between the two robust ground states (FE and PE) is an intermediate regime characterized by competing polar order with rotational degree of freedom of the polarization. It is then natural to ask how the photovoltaic properties are affected by the polar instability.

Photovoltaic property of La-substituted BFO

Plotted in Fig. 2 (A and B) (also in fig. S6A) are typical photovoltaic responses of the La-substituted BFO films with opposite polarization states under identical white-light illumination (detailed spectrum shown in fig. S7). The films with ferroelectric ground states exhibit switchable open-circuit voltage (V_{oc}) and short-circuit current density (J_{sc}), a typical behavior of a ferroelectric solar cell. In contrast, those films in antipolar/nonpolar states show negligible photovoltaic output, which confirms that the switchable photovoltaic effect originates from the remnant polarization. Furthermore, the positive and negative polar states produce almost symmetrical outputs with opposite signs, suggesting insignificant influence from the asymmetric top and bottom electrical contacts. As summarized in Fig. 2D, both V_{oc} and J_{sc} show large enhancements upon La substitution, and peak around the FE-PE phase transition, followed by a sharp drop due to the loss of polarization. Compared to pure BFO, the 20% La–substituted film shows at least one order of magnitude enhancement in J_{sc} and doubled V_{oc}. The enhancement is persistent, as revealed by the time-dependent J_{sc} test (Fig. 2C). Furthermore, all the samples show comparable dark conductivities, suggesting similar intrinsic transport and electronic behaviors (fig. S6B). The experimental observations thus far support that the polar instability enhances the FPV performance of BFO films. However, thorough investigations of the optical properties are required to understand the microscopic origin of the enhancement.

Optical transitions and dynamics of La-substituted BFO

We have performed spectroscopic ellipsometry studies on La-substituted BFO films, from which the dielectric functions are extracted (fig. S8). The derived absorption coefficient α is plotted in Fig. 3A. The arrows denote two major electronic transitions with absorption onsets at ≈2.2 and ≈2.7 eV. We can then model the optical transitions following Tauc's rule

$$\alpha h\nu = A(h\nu - E_g)^n$$

with photon energy $h\nu$, the scaling constant A, the bandgap energy E_g, and the transition type n ($n = 1/2$ for direct-allowed, 3/2 for direct-forbidden, 2 for indirect-allowed, and 3 for indirect-forbidden transitions, respectively) (30). Figure 3 (D to G) shows the Tauc plots in the form of $(\alpha h\nu)^{1/n}$ versus photon energy for direct- and indirect-allowed transitions. By extrapolating the linear part of the absorption curve to the abscissa, the transition energy can be determined according to the particular model used. It is established that the first transition of pure BFO (with the onset around 2.2 eV) originates from the CT instability intrinsic for iron oxides, in agreement with the dipole-forbidden p-d transition (fig. S9A) (31). With increasing La substitution, this transition branch becomes smeared and better described by an indirect-allowed transition model. The second optical transition at 2.7 eV coincides with the "direct" bandgap widely reported for BFO (32, 33). However, we found that this transition can be well fitted by both direct- and indirect-allowed transition models (fig. S10). It should be noted that at room temperature, the phonon absorption branch usually dominates the $(\alpha h\nu)^{1/2}$ plot (34). For pure BFO, the linear portions of the direct and indirect Tauc plots almost overlap with each other, implying that this electronic transition contains both direct and indirect features, which is consistent with the flatness of the valence band edge of BFO (35). La substitution results in effective separation of the direct and indirect portions around this transition, which is most pronounced at 20% concentration. It is observed that while the direct transition remains almost unchanged at ≈2.65 eV, the indirect transition strongly red-shifts with increasing La concentration (Fig. 3B). Moreover, if we integrate the spectral weight in the range of 1.9 to 3.1 eV, that is, roughly the light spectrum used in the photovoltaic measurements, then a substantial decreasing trend versus La substitution can be discerned (fig. S9B). All these observations point to the fact that La substitution makes the band-edge transitions more indirect, which directs us to look into the photocarrier dynamics in these films.

Time-resolved photocarrier dynamics were examined using transient reflectivity spectroscopy based on the pump-probe method. The pump pulse with photon energy of 3.1 eV mainly excites a CT transition from the strongly hybridized O 2p to Fe 3d states. Following the initial photoexcitation with a swift rise of $\Delta R(t)/R$ at $t = 0$, the carrier dynamics show three relaxation stages (36, 37): (i) The fast component (<1 ps) corresponds to the electron-phonon thermalization; (ii) the subsequent intermediate component (a few picoseconds) corresponds to the energy exchange between the lattice and spin system; and (iii) the slow, quasi-constant component (≈a few nanoseconds) is assigned to a combination of radiative recombination and heat diffusion out of the illuminated area of the sample (the latter effect should be negligible in this case because the sign of $\Delta R/R$ induced by heating is opposite to the experimental observation). This very slow relaxation is beyond the limit of our translation stage; however, the amplitude of the process reflects the degree of localization of the excited carriers in the vicinity of conduction band minima. Hence, the carrier dynamics can be well fitted by a
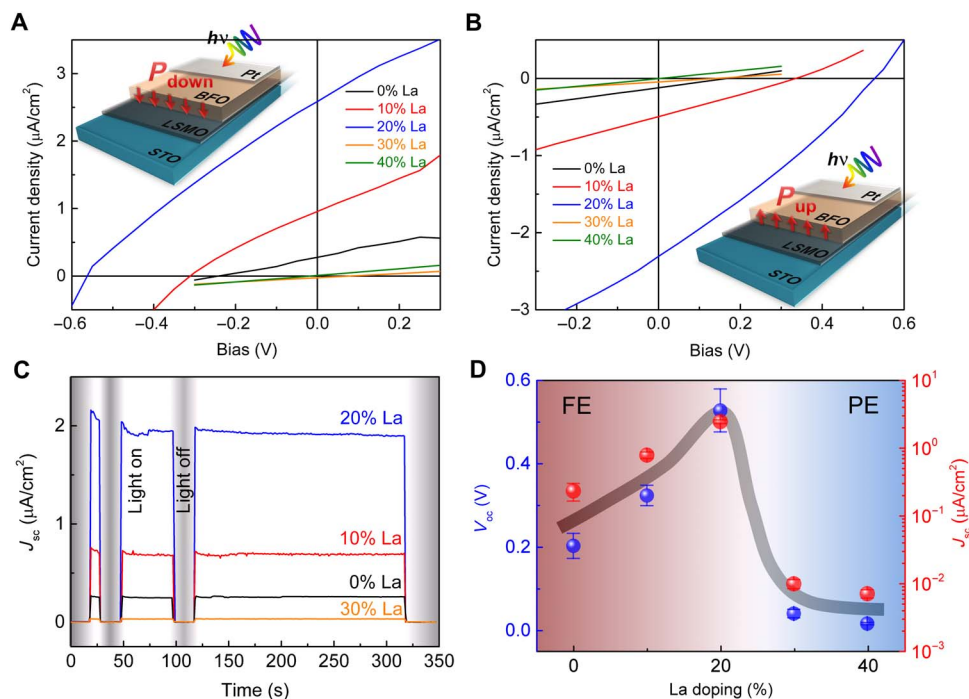
Fig. 2. Enhancement of photovoltaic effect of BFO by La substitution. Current density–voltage characteristics of La-substituted BFO films with (**A**) downward and (**B**) upward polarization states, respectively. The insets illustrate the device structure under test. (**C**) Time-dependent J_{sc} of different La-substituted BFO films. (**D**) Dependence of V_{oc} and J_{sc} on the La concentration, showing the progressive enhancement when approaching the phase transition boundary.

convolution of the Gaussian function $G(t)$ (laser pulse) with a biexponential decay function

$$\Delta R(t)/R = \left(A_1 \exp\left(\frac{-t}{\tau_{fast}}\right) + A_2 \exp\left(\frac{-t}{\tau_{inter}}\right) + A_3 \right) G(t)$$

where A_1, A_2, and τ_{fast}, τ_{inter} are the amplitudes and time constants of the fast and intermediate components, respectively. A_3 is the amplitude associated with the radiative recombination of present interest. In Fig. 3C, the normalized $\Delta R(t)/R$ persists over longer time spans for 20% La–substituted BFO. This result agrees with the increasing weight of indirect transitions in La-substituted BFO, as revealed in the absorption spectra.

Computational modeling

To better understand the effect of La substitution on the electronic structure of BFO, we turn to first-principles calculations using density functional theory (DFT). Figure 4A is the DFT-calculated band structure of pure BFO, showing the conduction band minimum (CBM) at the Γ point. The valence band maxima (VBM) at multiple k points have very similar energy, leading to a nearly direct bandgap. By increasing the La concentration, we find that the bandgap becomes more indirect, where the valence band energy differences between Γ and other k points become larger ($\Delta E = 75$ meV). Figure 4B shows the band structure calculated with three La atoms replacing Bi atoms in the 80-atom supercell (corresponding to 18.75% doping concentration). As shown in this band structure (Fig. 4B), the Γ point valence band energy decreases, while the valence band energies of other k points such as X and M increase, becoming the VBM. At finite temperature, the electron and hole populations will obey the Fermi-Dirac distribution. When the indirect and direct bandgaps differ by more

than the room temperature thermal scale (for example, the top of the valence bands at X and M points has higher energies than that of Γ point), most of the holes at equilibrium reside at X and M. Therefore, their recombination with excited electrons at the Γ point of the conduction band will be momentum-forbidden, leading to a slow recombination rate. This direct-to-indirect bandgap feature still allows for significant absorption within the visible energy range while reducing the electron-hole recombination rate because of the separation of the CBM and VBM in momentum space. This effect can be further quantified by computing the thermal population of the carriers and their lifetime enhancement, as shown in Fig. 4C, owing to the indirect bandgaps (section S1). By further increasing the La concentration, this direct-indirect bandgap effect should be more pronounced. However, high La concentrations diminish the ferroelectricity of the whole material, turn the sample into paraelectric, and result in the loss of the photocurrent.

Because of the lack of "lone-pair" s electrons, the La atom dopants have less ferroelectric off-center displacement than the host Bi atoms. Our DFT calculation shows ≈0.3 Å smaller displacement for La compared to Bi. Furthermore, this suppression reduces the nearby iron off-center displacement (reduced by ≈0.1 Å from DFT), creating a local region with different polarization magnitude and direction than the surrounding regions with pure BFO composition. These regions with suppressed polarization introduce local strain (Fig. 1H). In several materials, the presence of local strains is linked with direct-indirect bandgap transitions. Examples include single-layer MoSe₂ (38) and some bulk three-dimensional (3D) materials such as STO (39) and organometal-halide perovskites (40).

In our system, the electronic origin of the indirect bandgap is also the removal of lone-pair 6s electrons due to La substitution. In pure BFO, the VBM states of Γ point are mainly the antibonding states formed by the Bi s, Fe d, and O p orbitals. When La substitutes Bi, the missing
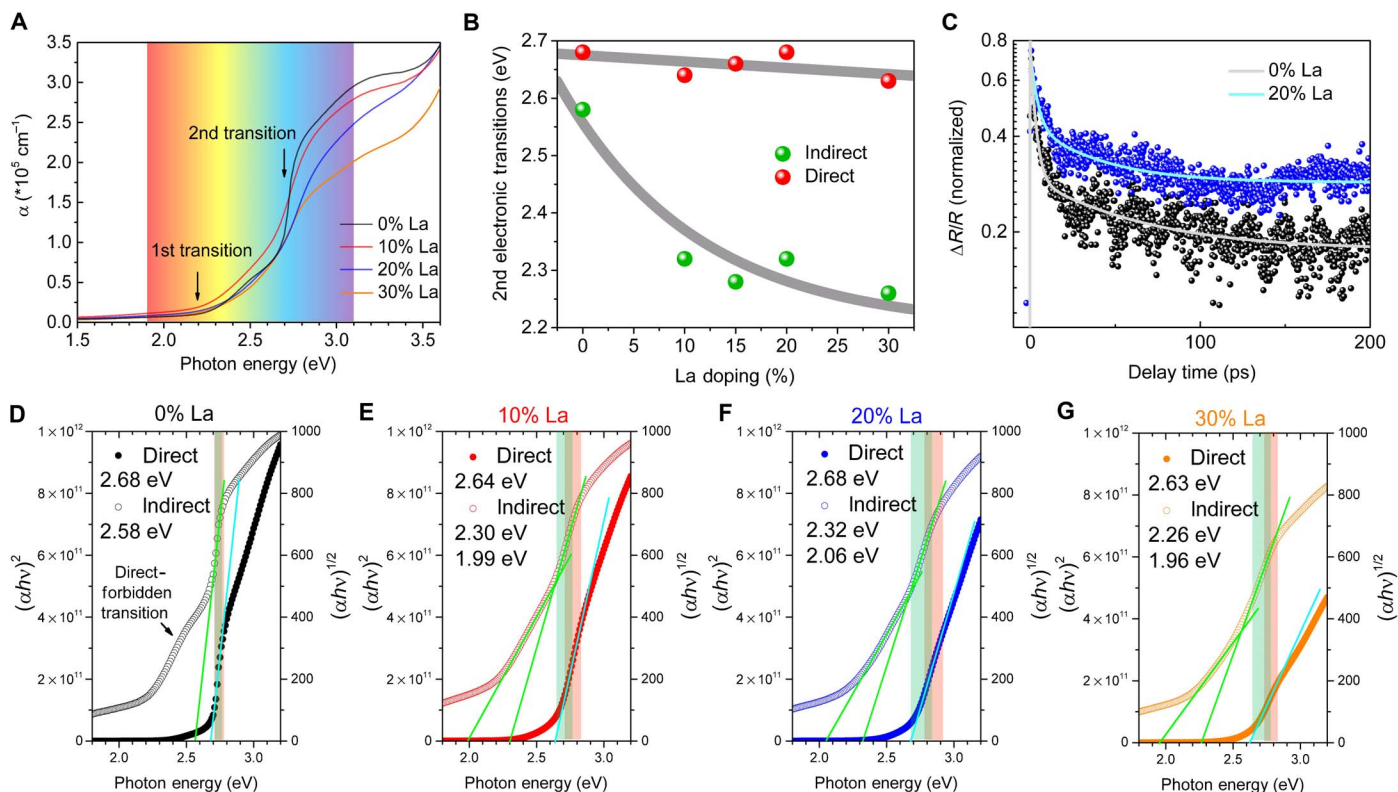
Fig. 3. Optical properties of La-substituted BFO. (**A**) Absorption coefficients of La-substituted BFO films determined by spectroscopic ellipsometry. The light spectrum used for photovoltaic measurements coincides with the visible light spectrum. (**B**) Calculated direct and indirect transition energies of the second electronic transition indicated in (A). (**C**) Transient reflectivity curves of 0 and 20% La–substituted BFO films fitted by biexponential functions plus a slow amplitude component for radiative recombination. (**D** to **G**) $(\alpha h\nu)^2$ and $(\alpha h\nu)^{1/2}$ Tauc plots of La-substituted BFO films used for determining the direct and indirect transition energies. The green and red shaded regions indicate regions satisfying indirect and direct transition models, respectively.

lone-pair electrons lower the energy of these antibonding VBM states at Γ. On the other hand, at other k points such as X and M, the valence wave functions have many nodes located at Bi sites. Substituting La at these nodal sites does not change the energies of the states at these k points significantly. Thus, increasing La concentration leads to a lowering of the VBM energy at Γ but not at other k points, resulting in an indirect bandgap. There are certain defect configurations where all La atoms substitute Bi atoms at non-nodal sites and lead to direct gaps. However, these configurations are uncommon and unlikely to occur systematically at room temperature.

DISCUSSION
Comprehensive understanding of the interplay between polar order, structural distortion, band structure, and optical transition requires a careful examination of the molecular orbitals (MOs) in BFO, as illustrated in Fig. 5A. The first and second electronic transitions denoted in Fig. 3A correspond to the weak dipole-forbidden $t_{1g}(\pi) \rightarrow t_{2g}(\pi^*)$ and strong dipole-allowed $t_{2u}(\pi) \rightarrow t_{2g}(\pi^*)$ p-d CT transitions, respectively (31). The nominally forbidden $t_{1g}(\pi) \rightarrow t_{2g}(\pi^*)$ transition becomes allowed because of the symmetry breaking of the FeO_6 octahedron. In BFO, the ferroelectric polarization originates from the large relative displacement of O_6 octahedron centers with respect to the Bi and Fe sublattices (Fig. 5B), which makes three Fe–O bonds shorter and the other three longer. The distortion of the FeO_6 octahedron consequently lifts the degeneracy of the $t_{1g}(\pi)$ orbital, which accounts for the absorp-

tion onset around 2.2 eV in pure BFO. This optical signature is a direct indicator of the CT instability ubiquitous for iron oxide insulators (31). By replacing Bi with La, the polar ground state is disturbed, with a tendency for polarization rotation toward $[001]_{pc}$ axis due to the symmetry change from rhombohedral in BFO toward orthorhombic in orthoferrites (26, 41). The rotational instability of the polarization is evidenced by the inhomogeneous in-plane PFM signals (fig. S4) in association with enhanced dielectric permittivity and dielectric loss for the La-substituted samples (fig. S2). In this process, although the material remains polar, continuous changes of the relative displacements between Fe^{3+}, Bi^{3+}, and O_6 sublattices are expected due to the inherent coupling between polarization and lattice. Although the exact symmetry and atomic coordinates of the intermediate phase are still debated (42), previous research suggested the reduction of the Fe off-centering in FeO_6 octahedra and changes in the Fe–O bond lengths (29), which are also observed in our theoretical modeling. Moreover, polarization rotation and symmetry change will induce a change in the octahedral tilt pattern, which influences the Fe–O–Fe bond angle. The cooperative lattice and polar instabilities hence influence orbital overlaps, create local strain, and change the energy splitting in momentum space, resulting in an indirect electronic transition. It is worth pointing out that at a composition close to the phase boundary (for example, 20% La), the existence of incommensurate phase implies a large spread of the polarization and structural order parameters (27), which explains the smearing of the optical band edge and an increase in the spectral weight of indirect transition. The tendency toward indirect bandgap in La-substituted
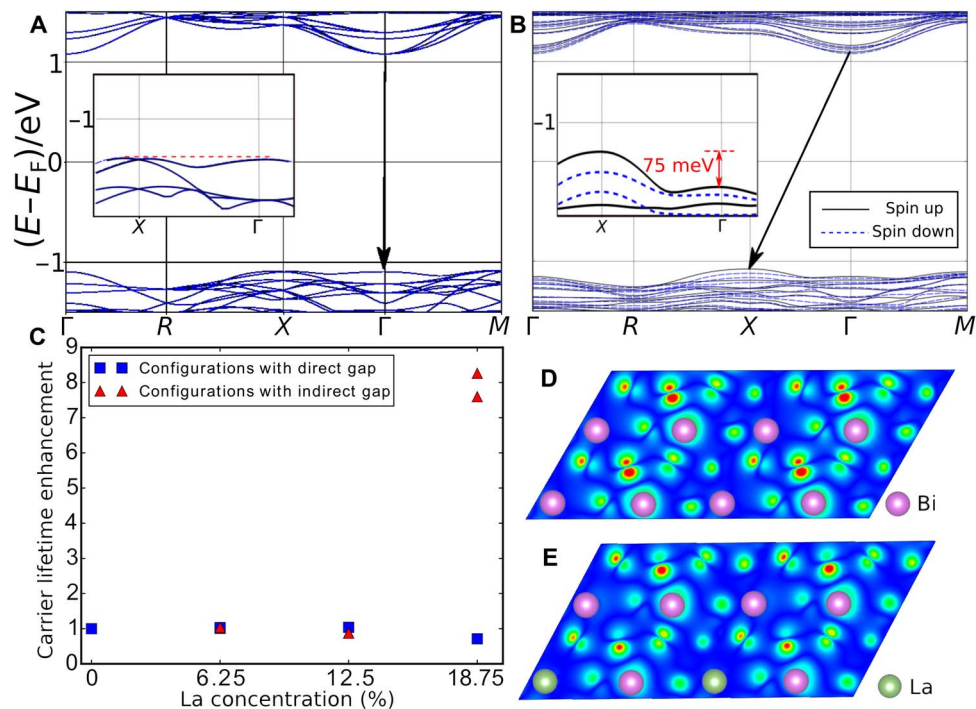
Fig. 4. First-principles calculations of La doping in BFO. (**A**) DFT-calculated band structure of pure BFO ($2 \times 2 \times 2$ supercell). The inset zooms in the valence band edge near X and Γ points, indicating nearly direct bandgap. (**B**) DFT-calculated band structure of 18.75% La–substituted BFO. The inset shows the indirect bandgap feature of the valence band edge at X and Γ points. (**C**) Carrier lifetime enhancement factor, calculated from DFT band structures, under different substitution concentrations and for different La defect configurations. When introducing more La into BFO, the band structures show more indirect bandgap features, leading to reduced recombination rate. In most configurations, La substitution results in an indirect gap. The blue square at 18.75% La illustrates an uncommon case with a direct gap. (**D**) Band charge density of [001] plane for VBM at X point in pure BFO, showing the nodal sites at middle Bi atoms. (**E**) Band charge density of [001] plane for VBM at X point in La-doped BFO with the same nodal site positions. In this case, La atoms occupy the wave function nodal sites, leaving the energy at this k point unchanged.

BFO coincides with the theoretical prediction showing a similar trend throughout the structural evolution from rhombohedral to orthorhombic to cubic (*43*). In addition, the indirect bandgap of LaFeO₃ also gives a hint on the direct-indirect gap transition (*44*). It is worth pointing out that because of the energy proximity between direct and indirect gaps, the optical absorption is weakly affected by the direct-indirect transition. However, the radiative recombination can be strongly suppressed by the indirect bandgap because of the fast thermalization of the electrons to the conduction minimum (Fig. 3C).

The phenomenon we have discussed is not unique to La. In fact, we have also tested other lanthanide substitutions such as Sm and Dy and observed the same enhancement in photovoltaic performance (fig. S11). Again, this enhancement is accompanied by the suppression of ferroelectric polarization and decreased polar stability (increased dielectric constant) in the substituted films (fig. S12). In the *B* site–doped BFO, similar polar instability also exists, as evidenced by the co-existence of polar and nonpolar domains in the $BiFe_{0.5}Cr_{0.5}O_3$ thin film (fig. S13), which may also contribute to its superior photovoltaic performance (*15*). The mechanism proposed here can conceptually be extended to other systems such as hybrid perovskite $CH_3NH_3PbI_3$, which contains dipolar molecule at the *A* site. Owing to the small energy barrier for molecular rotation (tens of millielectron volts), the orientations of the molecular dipoles are expected to be both spatially and dynamically disordered at room temperature (*45*). In a sense, La-doped BFO is similar to a dipole glass, while the dipolar molecules in

$CH_3NH_3PbI_3$ show more liquid-like behaviors. The rotation of the molecular dipoles could induce local disturbance to the inorganic framework via H-bond/van der Waals interaction, which, in turn, distorts the PbI_6 octahedra and modifies the electronic band edges. The effect may partially account for the direct-indirect characteristic of the bandgap and long carrier lifetimes in these hybrid perovskites (*40*, *46*). Furthermore, the dynamic dipole disorder also results in large dielectric permittivity up to high frequencies (terahertz) (*47*), which facilitates the charge carrier screening by forming large polarons after optical excitation, further suppressing the radiative recombination (*48*).

In summary, destabilizing the polar order in BFO significantly improves its FPV performance. The *A*-site chemical substitutions produce local disturbance to the ferroelectric ground state, triggering an overall tendency for polarization rotation in the system. This rotational instability modifies the local crystal field and band structure, which drives the direct-to-indirect transition of the bandgap. The indirect nature of the band-edge transition strongly suppresses the radiative recombination of the thermalized photoexcited carriers, thus improving the FPV effect, despite being coupled to loss of ferroelectric order. This approach offers a novel pathway for enhancing the photovoltaic performance in ferroelectrics and related materials via the intimate coupling between polarization, lattice, and orbital degree of freedoms. It also sheds some light onto the origin of very long carrier lifetimes in hybrid perovskites, in which the *A*-site dipoles are dynamically disordered.
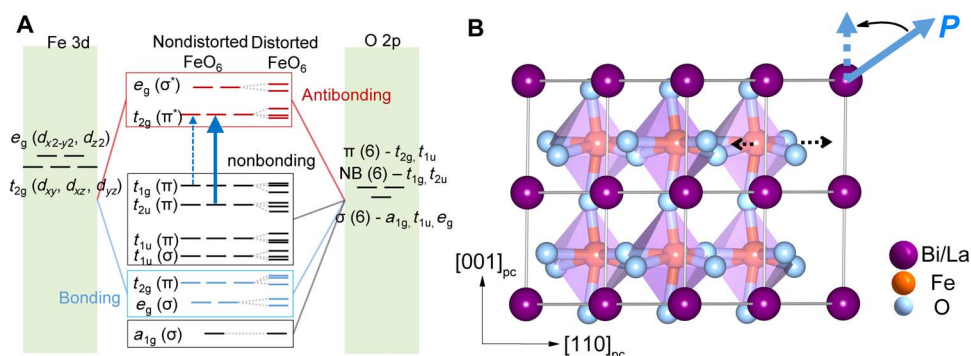
Fig. 5. MOs and lattice distortion of FeO$_6$. (**A**) Hybridization between 5 Fe 3d and 18 O 2p orbitals forms low-energy bonding (blue box), high-energy antibonding (red box), and intermediate nonbonding (black box) orbitals. The dashed arrow denotes weak dipole-forbidden transition, and the solid arrow denotes strong dipole-allowed transition. (**B**) Crystal structure of BFO with R_{3c} symmetry showing FeO$_6$ distortion and tilting pattern coupled to the ferroelectric polarization (blue solid arrow). The blue dotted arrow indicates the polarization rotation induced by A-site substitution. The black dotted arrows denote the displacive tendency of the Fe and O$_6$ relative to Bi sublattice in accordance with the polarization rotation path, that is, the in-plane polarization tends to diminish.

MATERIALS AND METHODS

Thin-film growth and photovoltaic cell fabrication

La$_{0.7}$Sr$_{0.3}$MnO$_3$ (LSMO) bottom electrodes and lanthanide-substituted (La, Sm, Dy) BFO films were sequentially grown by pulsed laser deposition on (001)-oriented STO substrates with 4° miscut along in-plane <110> direction. The large miscut angle was to ensure a ferroelectric monodomain state in the resulting films. Stoichiometric ceramic targets were used. The growth temperature and oxygen partial pressure were held at 800°C and 200 mtorr, respectively, for LSMO, and 650°C and 50 mtorr, respectively, for BFO films. The laser fluence was about 2 J/cm^2 for LSMO growth and about 1.2 J/cm^2 for BFO growth. The compositions of the films were checked using energy-dispersive spectroscopy to be within 3% error with regard to those of the corresponding targets, suggesting stoichiometric material transfer in the laser ablation. The thickness of the LSMO films was ≈15 nm, while that of the BFO films was ≈120 nm. Finally, 20-nm-thick square Pt electrodes (with visible transmittance of 10 to 15%) ranging from 20 × 20 μm^2 to 100 × 100 μm^2 were patterned on top of the BFO films either through a shadow mask or using photolithography.

Ferroelectric, dielectric, and photovoltaic measurements

All the electrical measurements were carried out on a micromanipulator probe station equipped with a heating stage. Ferroelectric properties were measured using a commercial ferroelectric tester (Precision LC, Radiant Technologies). Dielectric data were collected using a commercial impedance LCR meter (E4980A, Agilent). Photovoltaic responses were characterized by a picoampere meter/dc voltage source (4140B, Hewlett Packard) under ≈100 mW/cm^2 white light illumination from a halogen lamp (see fig. S7 for detailed spectrum). The irradiation intensity was carefully calibrated using a standard reference cell (91150V, Newport). To ensure the reproducibility of the results, at least 10 devices from two to three different batches of samples were tested for each doping concentration.

PFM measurement

PFM measurements were conducted under nonresonant mode on a commercial atomic force microscope (AFM) (Asylum Research MFP-3D) using a stiff Pt/Ir-coated silicon tip with a spring constant of 40 N/m. An ac voltage of 1 V with a frequency of 10 kHz was applied to the conductive tip, which drives the film surface to vibrate because of converse piezoelectric effect. The amplitude and phase of the vibration were then picked up by a lock-in amplifier. Here, PFM images were plotted using the signal of amplitude*sin(phase) (−90° ≤ phase ≤ 90°), of which the absolute value and sign reflect the polarization magnitude and direction, respectively.

Spectroscopic ellipsometry

The spectroscopic ellipsometry measurements were performed using a commercially available rotating analyzer instrument with compensator (V-VASE; J.A. Woollam Co. Inc.) within the spectral range from 0.6 to 6.5 eV. Data were collected at two angles of incidence (50° and 70°), and the complex dielectric function was determined on a wavelength-by-wavelength basis using a three-layer model comprising surface roughness, the La-substituted BFO, and the STO substrate (49). The absorption coefficient was then calculated from the dielectric function.

Transient reflectivity spectroscopy

We used the typical 1.55-eV pump/3.1-eV probe spectroscopy to investigate the La-substituted BFO samples. The light source was a commercial mode-locked Ti:sapphire laser (Spitfire Pro, Spectra-Physics) running at a repetition rate of 1 kHz, with a pulse width of 120 fs. Both the pump and the probe beams were focused on the surface of the sample with a spot diameter of about 250 μm. The pump beam with photon energy of 3.1 eV was obtained from a frequency-doubled fundamental beam (800 nm) in a 1-mm β-BaB$_2$O$_4$ crystal. The average pump fluence was about 2.4 mJ/cm^2, 30 times larger than that of the probe. The pump beam with a center wavelength of 400 nm was oriented at normal incidence to the sample surface, and the probe beam had an incident angle of about 6° from the surface normal.

Computational modeling

The plane-wave density functional package Quantum Espresso (50) was used to perform the structural relaxation and electronic structure calculation with the PBEsol exchange-correlation functional (51). Norm-conserving, designed nonlocal pseudopotentials were generated with the OPIUM package (52, 53). For the electrostatic potential calculation, the ferroelectric/paraelectric domains were built by stacking two hexagonal supercells (indicating ferroelectric and paraelectric phases, respectively) with around 33% La substitution concentration. For the electronic structure calculations, a 2 × 2 × 2 supercell of the rhombohedral BFO unit cell (80 atoms) was used to model different concentrations of La (0%, 6.25%, 12.5%, and 18.75%). A plane-wave kinetic

energy cutoff of 50 Ry and k point sampling on a $4 \times 4 \times 4$ grid were sufficient to yield converged total energies. Because of the well-known deficiency of DFT in overly delocalizing electrons, the DFT + U method was used, with effective U_{eff} applied on the Fe 3d orbitals for all the calculations. $U_{eff} = 4$ eV was shown to improve the structural relaxations significantly (28). In addition, as shown in (21), $U_{eff} = 5$ eV was optimal for the electronic structure calculations. Therefore, we used $U_{eff} = 4$ eV for the structural relaxation and $U_{eff} = 5$ eV to compute the electronic band structures. The structures with various La atom positions and doping concentrations were all fully relaxed with a force tolerance of 0.001 Ry/bohr. The band structures of the doped structures with low total energies were computed on a denser uniform k-point grid ($16 \times 16 \times 16$) to calculate their recombination rates.

SUPPLEMENTARY MATERIALS

Supplementary material for this article is available at http://advances.sciencemag.org/cgi/content/full/4/7/eaat3438/DC1

Section S1. Carrier lifetime enhancement due to indirect bandgap.
Fig. S1. Ferroelectric polarization characterizations of the La-doped BFO films.
Fig. S2. Dielectric characterization of the La-doped BFO films.
Fig. S3. Topographic and PFM images of the as-grown La-doped BFO films.
Fig. S4. Local polarization switching of the La-doped BFO films.
Fig. S5. Temperature-dependent P-E loops.
Fig. S6. Photocurrent and dark current of the La-doped BFO films.
Fig. S7. Spectrum of the halogen lamp used in the photovoltaic test.
Fig. S8. Optical dielectric constants.
Fig. S9. Direct-forbidden fitting and integrated spectral weight.
Fig. S10. Complete fittings of the absorption spectra using Tauc's rule.
Fig. S11. Universal polar instability–enhanced FPV effect.
Fig. S12. Evidence for polar instability in Dy-doped BFO.
Fig. S13. Evidence for polar instability in BiFe$_{0.5}$Cr$_{0.5}$O$_3$.
References (54–56)

REFERENCES AND NOTES

1. A. G. Chynoweth, Surface space-charge layers in barium titanate. *Phys. Rev.* **102**, 705–714 (1956).
2. A. M. Glass, D. von der Linde, T. J. Negran, High-voltage bulk photovoltaic effect and the photorefractive process in LiNbO$_3$. *Appl. Phys. Lett.* **25**, 233–235 (1974).
3. W. T. H. Koch, R. Munser, W. Ruppel, P. Würfel, Bulk photovoltaic effect in BaTiO$_3$. *Solid State Commun.* **17**, 847–850 (1975).
4. T. Choi, S. Lee, Y. J. Choi, V. Kiryukhin, S.-W. Cheong, Switchable ferroelectric diode and photovoltaic effect in BiFeO$_3$. *Science* **324**, 63–66 (2009).
5. W. Ji, K. Yao, Y. C. Liang, Bulk photovoltaic effect at visible wavelength in epitaxial ferroelectric BiFeO$_3$ thin films. *Adv. Mater.* **22**, 1763–1766 (2010).
6. D. Lee, S. H. Baek, T. H. Kim, J.-G. Yoon, C. M. Folkman, C. B. Eom, T. W. Noh, Polarity control of carrier injection at ferroelectric/metal interfaces for electrically switchable diode and photovoltaic effects. *Phys. Rev. B* **84**, 125305 (2011).
7. R. Guo, L. You, Y. Zhou, Z. S. Lim, X. Zou, L. Chen, R. Ramesh, J. Wang, Non-volatile memory based on the ferroelectric photovoltaic effect. *Nat. Commun.* **4**, 1990 (2013).
8. S. Y. Yang, J. Seidel, S. J. Byrnes, P. Shafer, C.-H. Yang, M. D. Rossell, P. Yu, Y.-H. Chu, J. F. Scott, J. W. Ager III, L. W. Martin, R. Ramesh, Above-bandgap voltages from ferroelectric photovoltaic devices. *Nat. Nanotechnol.* **5**, 143–147 (2010).
9. M. Alexe, D. Hesse, Tip-enhanced photovoltaic effects in bismuth ferrite. *Nat. Commun.* **2**, 256 (2011).
10. A. Bhatnagar, A. R. Chaudhuri, Y. H. Kim, D. Hesse, M. Alexe, Role of domain walls in the abnormal photovoltaic effect in BiFeO$_3$. *Nat. Commun.* **4**, 2835 (2013).
11. W. Ji, K. Yao, Y. C. Liang, Evidence of bulk photovoltaic effect and large tensor coefficient in ferroelectric BiFeO$_3$ thin films. *Phys. Rev. B* **84**, 094115 (2011).
12. W. S. Choi, M. F. Chisholm, D. J. Singh, T. Choi, G. E. Jellison Jr., H. N. Lee, Wide bandgap tunability in complex transition metal oxides by site-specific substitution. *Nat. Commun.* **3**, 689 (2012).
13. I. Grinberg, D. V. West, M. Torres, G. Gou, D. M. Stein, L. Wu, G. Chen, E. M. Gallo, A. R. Akbashev, P. K. Davies, J. E. Spanier, A. M. Rappe, Perovskite oxides for visible-light-absorbing ferroelectric and photovoltaic materials. *Nature* **503**, 509–512 (2013).
14. P. V. Balachandran, J. M. Rondinelli, Massive band gap variation in layered oxides through cation ordering. *Nat. Commun.* **6**, 6191 (2015).
15. R. Nechache, C. Harnagea, S. Li, L. Cardenas, W. Huang, J. Chakrabartty, F. Rosei, Bandgap tuning of multiferroic oxide solar cells. *Nat. Photonics* **9**, 61–67 (2015).
16. H. Matsuo, Y. Noguchi, M. Miyayama, Gap-state engineering of visible-light-active ferroelectrics for photovoltaic applications. *Nat. Commun.* **8**, 207 (2017).
17. H. T. Yi, T. Choi, S. G. Choi, Y. S. Oh, S.-W. Cheong, Mechanism of the switchable photovoltaic effect in ferroelectric BiFeO$_3$. *Adv. Mater.* **23**, 3403–3407 (2011).
18. V. M. Fridkin, Bulk photovoltaic effect in noncentrosymmetric crystals. *Crystallogr. Rep.* **46**, 654–658 (2001).
19. R. von Baltz, W. Kraut, Theory of the bulk photovoltaic effect in pure crystals. *Phys. Rev. B* **23**, 5590–5596 (1981).
20. S. M. Young, A. M. Rappe, First principles calculation of the shift current photovoltaic effect in ferroelectrics. *Phys. Rev. Lett.* **109**, 116601 (2012).
21. S. M. Young, F. Zheng, A. M. Rappe, First-principles calculation of the bulk photovoltaic effect in bismuth ferrite. *Phys. Rev. Lett.* **109**, 236601 (2012).
22. S.-E. Park, T. R. Shrout, Ultrahigh strain and piezoelectric behavior in relaxor based ferroelectric single crystals. *J. Appl. Phys.* **82**, 1804–1811 (1997).
23. J. B. Neaton, C. Ederer, U. V. Waghmare, N. A. Spaldin, K. M. Rabe, First-principles study of spontaneous polarization in multiferroic BiFeO$_3$. *Phys. Rev. B* **71**, 014113 (2005).
24. D. Kan, L. Pálová, V. Anbusathaiah, C. J. Cheng, S. Fujino, V. Nagarajan, K. M. Rabe, I. Takeuchi, Universal behavior and electric-field-induced structural transition in rare-earth-substituted BiFeO$_3$. *Adv. Funct. Mater.* **20**, 1108–1115 (2010).
25. C.-J. Cheng, D. Kan, S.-H. Lim, W. R. McKenzie, P. R. Munroe, L. G. Salamanca-Riba, R. L. Withers, I. Takeuchi, V. Nagarajan, Structural transitions and complex domain structures across a ferroelectric-to-antiferroelectric phase boundary in epitaxial Sm-doped BiFeO$_3$ thin films. *Phys. Rev. B* **80**, 014109 (2009).
26. D. Kan, V. Anbusathaiah, I. Takeuchi, Chemical substitution-induced ferroelectric polarization rotation in BiFeO$_3$. *Adv. Mater.* **23**, 1765–1769 (2011).
27. D. A. Rusakov, A. M. Abakumov, K. Yamaura, A. A. Belik, G. Van Tendeloo, E. Takayama-Muromachi, Structural evolution of the BiFeO$_3$–LaFeO$_3$ system. *Chem. Mater.* **23**, 285–292 (2011).
28. O. E. González-Vázquez, J. C. Wojdeł, O. Diéguez, J. Íñiguez, First-principles investigation of the structural phases and enhanced response properties of the BiFeO$_3$-LaFeO$_3$ multiferroic solid solution. *Phys. Rev. B* **85**, 064119 (2012).
29. D. V. Karpinsky, I. O. Troyanchuk, M. Tovar, V. Sikolenko, V. Efimov, A. L. Kholkin, Evolution of crystal structure and ferroic properties of La-doped BiFeO$_3$ ceramics near the rhombohedral-orthorhombic phase boundary. *J. Alloys Compd.* **555**, 101–107 (2013).
30. J. I. Pankove, *Optical Processes in Semiconductors* (Prentice-Hall, 1971), p. 422.
31. R. V. Pisarev, A. S. Moskvin, A. M. Kalashnikova, Th. Rasing, Charge transfer transitions in multiferroic BiFeO$_3$ and related ferrite insulators. *Phys. Rev. B* **79**, 235128 (2009).
32. S. R. Basu, L. W. Martin, Y. H. Chu, M. Gajek, R. Ramesh, R. C. Rai, X. Xu, J. L. Musfeldt, Photoconductivity in BiFeO$_3$ thin films. *Appl. Phys. Lett.* **92**, 091905 (2008).
33. J. F. Ihlefeld, N. J. Podraza, Z. K. Liu, R. C. Rai, X. Xu, T. Heeg, Y. B. Chen, J. Li, R. W. Collins, J. L. Musfeldt, X. Q. Pan, J. Schubert, R. Ramesh, D. G. Schlom, Optical band gap of BiFeO$_3$ grown by molecular-beam epitaxy. *Appl. Phys. Lett.* **92**, 142908 (2008).
34. P. K. Gogoi, D. Schmidt, Temperature-dependent dielectric function of bulk SrTiO$_3$: Urbach tail, band edges, and excitonic effects. *Phys. Rev. B* **93**, 075204 (2016).
35. S. J. Clark, J. Robertson, Band gap and Schottky barrier heights of multiferroic BiFeO$_3$. *Appl. Phys. Lett.* **90**, 132903 (2007).
36. Y. M. Sheu, S. A. Trugman, Y.-S. Park, S. Lee, H. T. Yi, S.-W. Cheong, Q. X. Jia, A. J. Taylor, R. P. Prasankumar, Ultrafast carrier dynamics and radiative recombination in multiferroic BiFeO$_3$. *Appl. Phys. Lett.* **100**, 242904 (2012).
37. Z. Zhang, Z. Jin, Q. Pan, Y. Xu, X. Lin, G. Ma, Z. Cheng, Temperature dependent photoexcited carrier dynamics in multiferroic BiFeO$_3$ film: A hidden phase transition. *Appl. Phys. Lett.* **104**, 151902 (2014).
38. S. Horzum, H. Sahin, S. Cahangirov, P. Cudazzo, A. Rubio, T. Serin, F. M. Peeters, Phonon softening and direct to indirect band gap crossover in strained single-layer MoSe$_2$. *Phys. Rev. B* **87**, 125415 (2013).
39. F. El-Mellouhi, E. N. Brothers, M. J. Lucero, I. W. Bulik, G. E. Scuseria, Structural phase transitions of the metal oxide perovskites SrTiO$_3$, LaAlO$_3$, and LaTiO$_3$ studied with a screened hybrid functional. *Phys. Rev. B* **87**, 035107 (2013).
40. C. Motta, F. El-Mellouhi, S. Kais, N. Tabet, F. Alharbi, S. Sanvito, Revealing the role of organic cations in hybrid halide perovskite CH$_3$NH$_3$PbI$_3$. *Nat. Commun.* **6**, 7026 (2015).
41. L. You, P. Caesario, L. Fang, P. Ren, L. Wang, Y. Zhou, A. Gruverman, J. Wang, Effect of lanthanum doping on tetragonal-like BiFeO$_3$ with mixed-phase domain structures. *Phys. Rev. B* **90**, 134110 (2014).
42. D. C. Arnold, Composition-driven structural phase transitions in rare-earth-doped BiFeO$_3$ ceramics: A review. *IEEE Trans. Ultrason. Ferroelect. Freq. Control* **62**, 62–82 (2015).
43. G. Catalan, J. F. Scott, Physics and applications of bismuth ferrite. *Adv. Mater.* **21**, 2463–2485 (2009).

44. M. D. Scafetta, A. M. Cordi, J. M. Rondinelli, S. J. May, Band structure and optical transitions in LaFeO₃: Theory and experiment. *J. Phys. Condens. Matter* **26**, 505502 (2014).

45. J. M. Frost, A. Walsh, What is moving in hybrid halide perovskite solar cells? *Acc. Chem. Res.* **49**, 528–535 (2016).

46. E. M. Hutter, M. C. Gélvez-Rueda, A. Osherov, V. Bulović, F. C. Grozema, S. D. Stranks, T. J. Savenije, Direct–indirect character of the bandgap in methylammonium lead iodide perovskite. *Nat. Mater.* **16**, 115–120 (2017).

47. I. Anusca, S. Balčiūnas, P. Gemeiner, Š. Svirskas, M. Sanlialp, G. Lackner, C. Fettkenhauer, J. Belovickis, V. Samulionis, M. Ivanov, B. Dkhil, J. Banys, V. V. Shvartsman, D. C. Lupascu, Dielectric response: Answer to many questions in the methylammonium lead halide solar cell absorbers. *Adv. Energy Mater.* **7**, 1700600 (2017).

48. K. Miyata, T. L. Atallah, X.-Y. Zhu, Lead halide perovskites: Crystal-liquid duality, phonon glass electron crystals, and large polaron formation. *Sci. Adv.* **3**, e1701469 (2017).

49. D. Schmidt, L. You, X. Chi, J. Wang, A. Rusydi, Anisotropic optical properties of rhombohedral and tetragonal thin film BiFeO₃ phases. *Phys. Rev. B* **92**, 075310 (2015).

50. P. Giannozzi, S. Baroni, N. Bonini, M. Calandra, R. Car, C. Cavazzoni, D. Ceresoli, G. L. Chiarotti, M. Cococcioni, I. Dabo, A. Dal Corso, S. de Gironcoli, S. Fabris, G. Fratesi, R. Gebauer, U. Gerstmann, C. Gougoussis, A. Kokalj, M. Lazzeri, L. Martin-Samos, N. Marzari, F. Mauri, R. Mazzarello, S. Paolini, A. Pasquarello, L. Paulatto, C. Sbraccia, S. Scandolo, G. Sclauzero, A. P. Seitsonen, A. Smogunov, P. Umari, R. M. Wentzcovitch, QUANTUM ESPRESSO: A modular and open-source software project for quantum simulations of materials. *J. Phys. Condens. Matter* **21**, 395502 (2009).

51. J. P. Perdew, A. Ruzsinszky, G. I. Csonka, O. A. Vydrov, G. E. Scuseria, L. A. Constantin, X. Zhou, K. Burke, Restoring the density-gradient expansion for exchange in solids and surfaces. *Phys. Rev. Lett.* **100**, 136406 (2008).

52. A. M. Rappe, K. M. Rabe, E. Kaxiras, J. D. Joannopoulos, Optimized pseudopotentials. *Phys. Rev. B* **41**, 1227–1230 (1990).

53. N. J. Ramer, A. M. Rappe, Designed nonlocal pseudopotentials for enhanced transferability. *Phys. Rev. B* **59**, 12471–12478 (1999).

54. J. Tauc, R. Grigorovici, A. Vancu, Optical properties and electronic structure of amorphous germanium. *Phys. Status Solidi B* **15**, 627–637 (1966).

55. F. Urbach, The long-wavelength edge of photographic sensitivity and of the electronic absorption of solids. *Phys. Rev.* **92**, 1324 (1953).

56. S. John, C. Soukoulis, M. H. Cohen, E. N. Economou, Theory of electron band tails and the Urbach optical-absorption edge. *Phys. Rev. Lett.* **57**, 1777–1780 (1986).

Citation: L. You, F. Zheng, L. Fang, Y. Zhou, L. Z. Tan, Z. Zhang, G. Ma, D. Schmidt, A. Rusydi, L. Wang, L. Chang, A. M. Rappe, J. Wang, Enhancing ferroelectric photovoltaic effect by polar order engineering. *Sci. Adv.* **4**, eaat3438 (2018).